Combinatorial Exploration and Mapping of Phase Transformation in a Ni−Ti−Co Thin Film Library

Naila M. Al Hasan, Huilong Hou, Tieren Gao, Jonathan Counsell, Suchismita Sarker, Sigurd Thienhaus, Edward Walton, Peer Decker, Apurva Mehta, Alfred Ludwig, and Ichiro Takeuchi*

ABSTRACT: Combinatorial synthesis and high-throughput characterization of a Ni−Ti−Co thin film materials library are reported for exploration of reversible martensitic transformation. The library was prepared by magnetron co-sputtering, annealed in vacuum at 500 °C without atmospheric exposure, and evaluated for shape memory behavior as an indicator of transformation. Composition, structure, and transformation behavior of the 177 pads in the library were characterized using high-throughput wavelength dispersive spectroscopy (WDS), X-ray photoelectron spectroscopy (XPS), X-ray diffraction (XRD), and four-point probe temperature-dependent resistance ($R(T)$) measurements. A new, expanded composition space having phase transformation with low thermal hysteresis and Co > 10 at. % is found. Unsupervised machine learning methods of hierarchical clustering were employed to streamline data processing of the large XRD and XPS data sets. Through cluster analysis of XRD data, we identified and mapped the constituent structural phases. Composition−structure−property maps for the ternary system are made to correlate the functional properties to the local microstructure and composition of the Ni−Ti−Co thin film library.

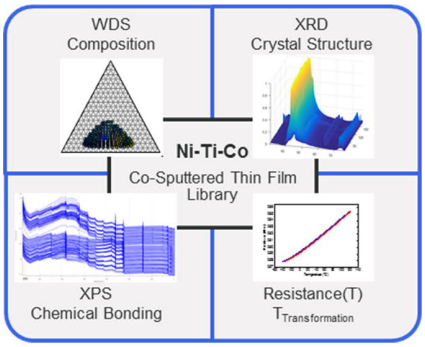

KEYWORDS: *Ni−Ti−Co, shape memory alloys, elastocaloric cooling, property mapping, machine learning, cluster analysis*

■ INTRODUCTION

Shape memory effect (SME) is a property that allows shape memory alloys (SMAs) to regain their shape when deformed through application of stress or temperature. The underlying mechanism is a reversible, diffusion-less, first-order martensitic transformation between two crystallographic phases.[1] The high temperature, high symmetry cubic phase is called austenite. The low temperature, low symmetry phase is called martensite, which can be present as twinned, detwinned, or a mixture of both in monoclinic and orthorhombic variants.[1] The temperatures at which transformation from martensite to austenite begins and ends are called A_s and A_f whereas the temperatures for the reverse pathway are marked by M_s and M_f. A cosputtered Ni−Ti−Co thin film library is investigated for SME through the evaluation of the phase transformation. First reported in 1975,[2] the Ni−Ti−Co alloy has since found wide applications: as a component of permanent magnets,[3−5] high-entropy alloys,[6,7] shape memory alloys,[8] and superalloys[9,10] along with substantive use in biomedical applications.[11−21] The addition of Co to NiTi has been shown to reduce the M_s and A_s temperatures in combination with the Ni content; it has also been shown to increase yield strength.[22,23] These improvements are sought out in elastocaloric cooling technology where ambient transition temperatures and small thermal hysteresis are desired.[24] Until now, investigations on the structural phases, mechanical properties, elastic properties, and phase transformation behavior that have been reported for Ni−Ti−Co involved one-by-one bulk preparation that covered a limited composition space, with addition of Co investigated only up to 10 at. %.[25,21,26−34] A more comprehensive study of the ternary system by Zhou et al., to determine the liquidus surface projection at 1373 K also involved one-by-one bulk preparation of 35 alloys. They evaluated the microstructure and different crystallographic phases present but did not report on the mechanical or transformation properties of Ni−Ti−Co.[35] To the best of the authors' knowledge, no systematic investigations of phase transformation in Ni−Ti−Co alloys, both in bulk and in the thin-film form that probes a greater composition space, have been reported thus far. Hence, this study aims to fill this information gap in identifying composition regions having martensitic phase transformation, with a focus on small thermal hysteresis.

We employ combinatorial materials science to facilitate a rapid investigation for the discovery, design, and development of new materials. It involves the correlation between physical

properties and composition through concurrent sample synthesis and high-throughput experimentation (HTE).[36] Combinatorial thin film synthesis allows access to a greater number of compositions than previously explored.[37] When combined with high-throughput characterization techniques, a systematic evaluation of parameters of interest can be carried out to fine-tune the functionalities of materials. Promising compositions can then be scaled up for bulk studies.

To quickly identify the compositions that transform in the ambient temperature range, a Ni−Ti−Co composition spread was synthesized using magnetron co-sputtering, and its composition−structure−property was mapped with high-throughput characterization. Unsupervised machine learning methods were used to both manage the large data sets acquired and analyze them efficiently.[38,39] The composition was determined using wavelength dispersive spectroscopy (WDS). We also evaluated the use of X-ray photoelectron spectroscopy (XPS) as a high-throughput chemical characterization technique; an automated, typical WDS measurement of a 177-sample library takes about 6 h whereas total acquisition time for XPS survey scans for the same sample library requires only half the time. Although surface effects and corrosion behavior of NiTi-based bulk as well as thin-film systems have been previously studied with XPS,[11,40−43] we report on systematic high-throughput XPS characterization and an indexed spectral database for Ni−Ti−Co. Using synchrotron X-ray diffraction (XRD) and high-throughput four-point probe temperature-dependent resistance $R(T)$ measurements, we report on the microstructure, phase diagram, and martensitic transformation behavior of Ni−Ti−Co alloys. We also report on phase transformation in compositions beyond $Ni_{50-x}Ti_{50}Co_x$ (x = 0 to 10 at. %). Furthermore, we identified a composition space with small thermal hysteresis (ΔT) that is promising for higher transformation efficiency and long-term stability.

RESULTS AND DISCUSSION

Figure 1 shows a ternary elemental plot of the compositional range covered in this study. With an x-y scanning table and characterization tools, the library was spatially analyzed, which offers another way to visualize data. Images of the materials library and corresponding labeled wafer positions are shown in the Supporting Information, Figure S1, parts a and b, respectively. Throughout the paper, we will use both methods to facilitate understanding of the different insights; experimental details are provided at the end.

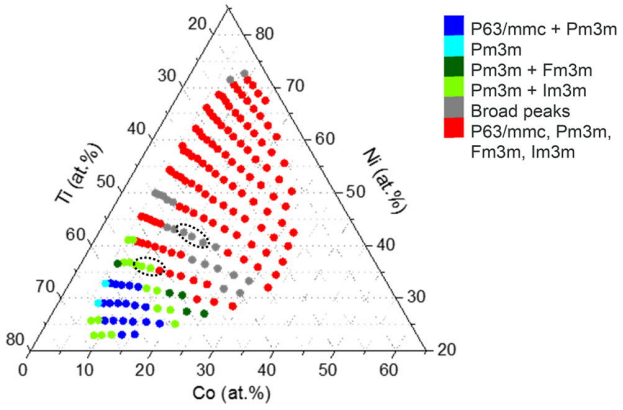

Figure 1. Ternary plot of Ni, Ti, and Co determined from high-throughput WDS. Compositions are grouped by color based on results for crystallographic phases from the Pearson correlation coefficient (PCC) hierarchical clustering model. Compositions grouped inside gray ellipses were determined to transform through an intermediate structure.

Characterization of Chemical Composition. Chemical composition determined from WDS shows elemental concentrations of 22.8 at. % < C_{Ni} < 72.8 at. %, 17.6 at. % < C_{Ti} < 68.2 at. %, and 5.4 at. % < C_{Co} < 33.2 at. %. Distribution of the elements by wafer position is shown in Figure S2a−c; these match the physical configuration of the targets inside the deposition chamber. The center of this library on the wafer has a composition of $Ni_{46.2}Ti_{40.1}Co_{13.7}$. Compositions with the highest and lowest Ni content are $Ni_{72.6}Ti_{18.6}Co_{8.8}$ and $Ni_{23}Ti_{68}Co_9$, highest and lowest Ti are $Ni_{23}Ti_{68}Co_9$ and $Ni_{67.5}Ti_{17.7}Co_{14.8}$, and highest and lowest Co are $Ni_{34.4}Ti_{32.5}Co_{33.1}$ and $Ni_{45.5}Ti_{49}Co_{5.5}$, respectively. Additionally, we obtained crystallographic evidence for carbide and oxide phases of Ti. Chemical composition data from WDS and XPS agree qualitatively for Ni and Ti distributions shown in Figure S2a,b and Figure S2d,e. Slight difference observed in the spatial distribution of Co (Figure S2, parts c and f) may be associated with a surface energy effect as XPS captures chemical activity present in the top 10 nm. In addition to differences in sampling depths, the variation in Co distribution may also be due to local surface aggregation of Co for a particular alloy blend. Despite the reduction in measurement time from XPS, we use WDS compositions going forward due to its higher accuracy and precision in quantifying elemental content. We do, however, use oxidation state mapping from XPS to understand crystallographic trends in the following sections.

Transformation Temperature Determination with Four-Point Probe Measurements. Compositions in the library were screened for phase transformation using a custom high-throughput four-point probe measurement system as measurable electrical changes accompany crystal structural changes during phase transformation.[44,45] We successfully identified compositions with phase transformation and narrow ΔT in the ambient temperature range. Film sheet resistance as a function of temperature, $R(T)$, was measured between −40 and +120 °C. Austenitic start (A_s), austenitic finish (A_f), martensitic start (M_s), and martensitic finish (M_f) temperatures were determined by applying the tangent method to the $R(T)$ curves, as demonstrated in the inset of Figure 2a. The first-order martensitic transformation is associated with a thermal hysteresis (ΔT) that reduces the reversibility of the transformation. This hysteresis is a result of energy dissipation due to frictional work and plastic accommodation during lattice distortions.[46−49] The hysteresis width determines the energy loss and inefficiency of the transformation such that a narrow width favors sustained reversibility.[50] Thermal hysteresis is determined by the difference between austenitic finish (A_f) and martensitic start (M_s) temperatures.

The $R(T)$ curves obtained can be divided into three categories—(1) linear, non-transforming curves with increasing slopes, (2) nonlinear, transforming curves (Figure 2a), and (3) linear, non-transforming curves with decreasing slopes (examples are highlighted with a black box in Figure S3). Linear $R(T)$ curves with increasing slopes showing no transformation were obtained for most of the library. Of the 177 compositions measured, 31 were observed to have reversible transformation behavior and hence, shape memory effect; these are listed by ascending Ni content in Table 1.

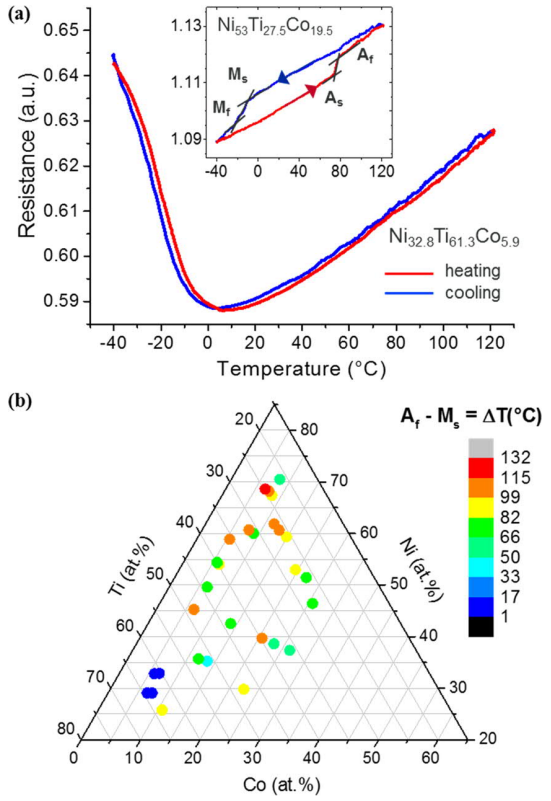

Figure 2. (a) $R(T)$ curve for $Ni_{32.8}Ti_{61.3}Co_{5.9}$ showing near-zero thermal hysteresis. Inset shows the tangent method to determine phase transformation temperatures A_s, A_f, M_s, and M_f from $R(T)$ curve for $Ni_{53}Ti_{27.5}Co_{19.5}$ alloy showing reversible phase transformation with large thermal hysteresis. (b) Distribution of thermal hysteresis $\Delta T = A_f - M_s$ in °C as a function of composition. Color scale bar from blue to red indicates small to large temperature widths.

Composition regions with SME at Co content greater than 10 at. % were identified for the first time. SME was observed in an elemental range for Ni from 25.8 to 70.5 at. %, Ti from 21.4 to 64.3 at. %, and Co from 5.5 to 26.4 at. %, respectively. Temperature ranges observed for martensite start, austenite finish and thermal hysteresis were $-25.2\ °C < M_s < 106.5\ °C$, $-23.2\ °C < A_f < 140.4\ °C$, and $0.7\ °C < \Delta T < 131.2\ °C$, respectively. Distribution of thermal hysteresis is shown in Figure 2b. Four compositions with $5.9\ at.\% < C_{Co} < 18.3\ at.\%$ were observed to have ΔT between 0.5 and 2.1 °C with the higher Co composition transforming at higher temperatures (M_s = 106.5 °C, A_f = 107.9 °C). Average A_f and M_s temperatures are around 79.6 and 14.4 °C, respectively, which are essential for SMA use in ambient temperatures. Some transformation pathways were incomplete in the evaluated range as seen from the missing M_s values in Table 1. These results are important as SME has been reported in bulk compositions of $Ti_{50}Ni_{50-x}Co_x$ (x = 2, 4, 6, and 8) but not observed for $Ti_{50}Ni_{40}Co_{10}$ measured at liquid nitrogen temperature.[14,29] Addition of Co preferentially substitutes Ni up to 14 at. % which has been shown to reduce the M_s. Although only a slight reduction in M_s is observed, our observations are overall in agreement with previous reports demonstrating addition of Co to reduce A_s and M_s through substitution of Ni.[23] Seven compositions were determined to have phase transformation through an intermediate structure (dotted gray ellipses, Figure 1a). These are not listed in the table as additional nanocharacterization measurements and temperature-dependent XRD are needed to verify these observations. Nonetheless, a two-step transformation has been previously reported for bulk Ni–Ti–Co and is also well-known to occur in NiTi as well as ternary systems such as TiNiCu, TiNiFe, and TiNiMo.[25,51−55]

Table 1. Composition, Martensitic Start (M_s), Austenitic Finish (A_f), and Thermal Hysteresis (ΔT) Determined from $R(T)$ for Ternary Ni–Ti–Co SMA Library by Ascending Ni Content

at. %			°C		
Ni	Ti	Co	M_s	A_f	$A_f - M_s = \Delta T$
25.8	63.5	10.7	−10.3	73.1	83.5
29.1	64.3	6.6	−25.2	−23.2	2.0
29.1	63.5	7.4	–	−8.3	8.3
29.8	47.7	22.5	–	83.9	83.9
32.8	61.3	5.9	−4.9	−2.8	2.1
32.9	60.4	6.7	−15.0	−14.3	0.7
35.2	51.2	13.6	58.0	95.8	37.9
35.7	52.4	11.9	–	79.6	79.6
37.3	36.3	26.4	0.8	61.1	60.3
38.6	38.3	23.1	15.5	79.4	64.0
39.7	39.7	20.6	10.6	109.9	99.3
42.5	43.6	13.9	–	72.9	72.9
45.3	48.4	6.3	−8.8	95.9	104.7
46.4	27.9	25.7	2.0	81.9	79.9
49.6	44.0	6.4	40.4	116.8	76.4
51.4	26.4	22.2	1.3	78.6	77.2
53.0	27.5	19.5	−12.8	78.5	91.3
54.0	39.8	6.2	22.8	109.7	86.9
54.4	40.0	5.7	24.8	94.2	69.4
58.9	35.6	5.5	29.7	140.4	110.6
59.3	25.8	14.9	0.7	95.8	95.0
59.5	22.2	18.3	106.5	107.9	1.5
60.0	31.0	9.0	19.3	99.0	79.7
60.7	26.4	13.0	−2.4	104.8	107.2
60.7	31.4	7.9	3.3	105.3	102.0
61.8	26.6	11.5	−6.3	104.3	110.6
65.3	27.9	6.8	73.5	111.0	37.5
67.4	24.2	8.4	16.1	104.0	87.8
68.2	24.3	7.5	5.2	107.7	102.6
68.6	24.7	6.6	−24.9	106.2	131.2
70.5	21.4	8.2	19.6	69.5	49.9

Crystal Structure and Phase Determination. We employed an unsupervised machine learning algorithm to determine a phase map for the Ni–Ti–Co library. Hierarchical cluster analysis using the Pearson correlation coefficient (PCC) was performed on high-throughput synchrotron XRD patterns (Figure S5a), collected at room temperature for the 177 annealed compositions, which delineates and separates compositions based on differences or similarities in their diffraction patterns. This also allows us to rapidly determine composition-structure relationships in the Ni–Ti–Co materials library.

The MATLAB-based data visualization platform Combi-View allows linking of sample composition with its XRD and XPS spectral patterns (Figure S4) and was used to perform the hierarchical cluster analysis on the XRD data (Figure S5).[56] An initial cluster analysis resulted in 32 groups. Upon refining and combining cluster groups based on number of low intensity peaks, six groups were determined consisting of 16 phases (see

space group in Table 2). Representative XRD patterns were analyzed using EVA4 XRD software from Bruker and matched against the International Centre for Diffraction Data (ICDD) database.[57] Results of the cluster analysis and phase distribution in a ternary composition plot are shown in Figure S5b,c and Figure 1, respectively. Selected diffraction patterns representing phases present in the six groups defined by PCC are shown in Figure 3. Crystal structures identified in this alloy library are listed in Table 2. Depending on where a composition was in the thermal cycle of the transformation, we expected to identify cubic, monoclinic, or orthorhombic structures for compositions exhibiting phase transformation.

Table 2. Crystal Structures Identified in the Ni–Ti–Co Thin Film Materials Library[a]

formula	space group	space group number	prototype
$(CoNi_2)Ti$	*P*63/*mmc*	194	hexagonal
$(Co_{0.15}Ni_{0.85})Ti$	*Pm*3*m*	221	
$(Co_{0.5}Ni_{0.5})Ti$	*Pm*3*m*	221	
$(Co_5NiTi_4)_{0.2}$	*Pm*3*m*	221	
$(Ni_{0.875}Co_{0.125})Ti$	*Pm*3*m*	221	
	*I*4/*mmm*	139	tetragonal
			$Al(Cr_{1.818}Ti_{0.182})$
			$Al(Cr_{1.818}Nb_{0.182})$
CoO	*Fm*3*m*	225	
CoTi	*Pm*3*m*	221	
Co_2GeTi	*Fm*3*m*	225	
Co_2NiTi	*Fm*3*m*	225	Co_2NiGa
			FeNi
			$MgNi_2Sn$
Co_2Ti_4O	*Fd*3*m*	227	
Co_3Ti_3O	*Fd*3*m*	227	
	*Iba*2	45	orthorhombic
			$Cr_{0.9585}Ga_2Sb_2$
	*P*1*m*1	6	monoclinic
			FeNi
NiTi	*P*21/*m*	11	monoclinic
NiTi	*P*3	147	hexagonal
NiTi	*Pm*3*m*	221	
$NiTi_2$	*Fd*3*m*	227	
$Ni_{1.02}Ti_{0.98}$	*Pm*3*m*	221	
Ni_2Ti	*R*3*m*	166	rhombo.h.axes
Ni_2Ti_4O	*Fd*3*m*	227	
Ni_4Ti_3	*R*3	148	rhombohedral
	*I*4/*m*	87	Tetragonal
			Ni_4W
$Ti(Co_{1.5}Ni_{1.5})$	*P*63/*mmc*	194	CoMnSn
TiC	*Fm*3*m*	225	TiCoNiSn
TiCo	*Pm*3*m*	221	
$Ti_4Ni_2O_{0.3}$	*Fd*3*m*	227	
	*F*43*m*	216	$(CoNi)Sn_2Ti_2$
			Ti_2NiAl
	*Im*3*m*	229	NiV
			TiV
	Pmam	51	orthorhombic
			$TiNi_{0.8}Cu_{0.2}$
	Pmmn	59	orthorhombic
			$NbNi_3$

[a]The default crystal structure type is cubic unless specified otherwise under prototype.

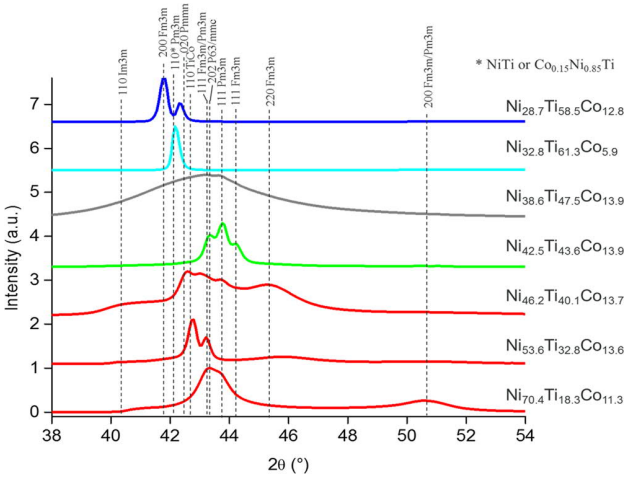

Figure 3. Selected X-ray diffraction patterns (wafer positions 94, 172, 91, 90, 89, 87, and 82 from top to bottom) representing phases present in the six clusters identified by PCC arranged in ascending Ni content. Patterns are offset for clarity.

Most common crystal type present was cubic austenite structure *Pm*3*m* in the form of NiTi or $Co_{0.15}Ni_{0.85}Ti$ crystal types and present in a single phase in only two compositions, $Ni_{29.1}Ti_{64.3}Co_{6.6}$ and $Ni_{32.8}Ti_{61.3}Co_{5.9}$ (positions 163 and 172, light blue cluster in Figure 1)—both of these also had near-zero thermal hysteresis $R(T)$ curves. The *Pm*3*m* phase is present predominantly in a mixture with other cubic phases *Im*3*m* and *Fm*3*m*, shown as dark green, light green, and red groups in Figure 1. These were observed to have linear, non-transforming $R(T)$ curves (Figure S3). For compositions in the Ni-rich region, mixed phases of hexagonal (prototype Ni_4In) and cubic (prototypes TiV, Co_2NiGa, $Co_{0.5}Ni_{0.5}Ti$, and $GaTiCo_2$) crystal structures were present, seen in red in Figure 1. Rhombohedral Ni_2Ti and Ni_4Ti_3 structures were also identified, and it was noted that NiTi is present in cubic, monoclinic, and hexagonal forms. For compositions with SME discussed in the previous section, both single phase and a mixture of cubic with orthorhombic structures were identified as seen from light and dark blue patterns in Figure 3. A mixture of hexagonal NiTi and cubic $(Co_5NiTi_4)_{0.2}$ for $Ni_{32.9}Ti_{60.4}Co_{6.7}$ (wafer position 162) also exhibited transformation with near-zero thermal hysteresis. It is important to note that this is a qualitative, not a quantitative assignment. Similarly, for $Ni_{42.5}Ti_{43.6}Co_{13.9}$(wafer position 90), where a potential two-step transformation was observed, a mixture of hexagonal $Ti(Co_{1.5}Ni_{1.5})$ and cubic *Pm*3*m*, *Im*3*m* structures of the prototypes $Co_{0.807}Ge_{0.123}W_{0.070}$ and $Cr_{0.875}Ti_{0.125}$ were identified. Since our library explores a composition space not yet reported, these and other prototype structures listed in the table provide an understanding of the type of crystal structures that may be present as we could not match every XRD peak with a listing in the ICDD. Finally, the gray cluster in Figure 1 is defined by a non-crystalline phase in which broad peaks were observed in the 2θ range of 40° to 48° (gray pattern in Figure 3) that corresponded with linear, non-transforming $R(T)$ curves characterized by decreasing slopes. This gray cluster forms a phase boundary separating NiTi–$NiTi_2$ double phase for compositions rich in Ti (dark blue in Figure S5c), which follows a distribution of Ti^{4+} peak observed from XPS mapping (Figure S6). Although no clear relationship could be drawn between variation of Ni or Co content with phase trans-

formation, crystallographic evidence for SME could be established, in agreement with theoretical and experimental observations reported in the literature.[11−13,28,35,54] These results also build on the challenging work associated with determining stable intermediate phases.[33]

DISCUSSION

To understand the relationship between composition, structure, and phase transformation, we can now align the data for material properties of the Ni−Ti−Co library across the chemical composition space. Phase transformation was observed in different parts of the composition plot with very little apparent connection to elemental variation. Of all the cubic space groups, transforming compositions are comprised of the *Pm*3*m* type in single phase or in mixture with *Fm*3*m*. While other compositions have similar crystal structures, they do not undergo transformation; this may be due to the presence of other crystal types such as non-transforming cubic and hexagonal phases. It is also difficult to determine the exact influence of composition on the presence of a particular crystal type since these are not single phases. Furthermore, the presence of additional phases may demand greater energy for the SME phase to transform, thereby increasing the thermal hysteresis width. This is supported by stable $R(T)$ curves having near zero thermal hysteresis for compositions $Ni_{29.1}Ti_{64.3}Co_{6.6}$ and $Ni_{32.8}Ti_{61.3}Co_{5.9}$ at positions 163 and 172 with a single crystal phase of NiTi or $Co_{0.15}Ni_{0.85}Ti$ types. Fabricating a materials library having smaller concentration gradients and centered around the composition space identified to have narrow hysteresis coupled with temperature-dependent XRD measurements may better elucidate the crystal phase composition of the transforming samples. Additionally, while scale-up of these compositions to verify the narrow thermal hysteresis in bulk is needed, thin films of Ni−Ti−Cu and Ni−Ti−Cu−V have been successfully scaled up and tested over many cycles.[58,59] Abrupt changes in $R(T)$ curves are also observed from one measurement area to the next such that they have linear and/or non-linear curves characterized by decreasing slopes from left to right (Figure S3). A cluster of XRD patterns reflects a similar distribution across the wafer and forms a phase boundary separating NiTi−$NiTi_2$ double phase for compositions rich in Ti (Figure S5c). XPS mapping of the Ti^{4+} peak across the wafer further confirms this observation (SI Figure S6). It may be that the annealing time is not long enough to produce large enough crystallites in this area of the materials library. Overall, while it is difficult to draw a definitive relationship between variation of Ni or Co content with phase transformation, we establish crystallographic evidence for SME, in agreement with observations already reported in literature for other Ni−Ti−Co alloys.[11−13,28,35,54] Nonetheless, these results expand on the challenging work of determining stable intermediate phases reported previously.[33]

CONCLUSION

A combinatorial Ni−Ti−Co thin film materials library covering a large composition space was synthesized using magnetron cosputtering and annealed at 500 °C for 1 h in vacuum. Large data sets of composition, transformation temperatures, and crystal structure were obtained from high-throughput WDS and XPS, four-point probe temperature-dependent resistance, and synchrotron XRD measurements that enabled rapid materials characterization and screening. Transformation temperatures were probed in the −40 to +120 °C range to screen for shape memory alloys that could be used in ambient temperature applications. By employing combinatorial synthesis and high-throughput experimentation, we demonstrate the effectiveness of the methodology in systematically mapping phase transformation and drawing composition-structure−property relationships. Cross sample position analysis between and within data sets allowed for greater insights, and the following observations were drawn:

- Chemical composition space bounded between 22.8 at. % < C_{Ni} < 72.8 at. %, 17.6 at. % < C_{Ti} < 68.2 at. %, and 5.4 at. % < C_{Co} < 33.2 at. % was synthesized.
- Phase transformation was observed in compositions beyond the range previously reported as $Ni_{50-x}Ti_{50}Co_x$ (x = 0 to 10 at. %), with Co concentration between 5 and 26 at. %.
- A new compositional region having narrow thermal hysteresis (ΔT between 0.5 and 2 °C) centered around 6 at. % Co in Ti-rich regions was identified.
- Transforming compositions are composed of mixtures of cubic structures from *Pm*3*m* and *Fm*3*m* space groups as well as orthorhombic and hexagonal structures.
- Non-transforming compositions were characterized by crystalline mixtures of multiple cubic *Pm*3*m* phases, *Pm*3*m* with *Fm*3*m* along with *Im*3*m* cubic phases in addition to non-crystalline phases defined by broad XRD peaks around 2θ = 40°.
- Alloys with distinct XRD patterns for a single cubic phase showed near-zero thermal hysteresis.
- Large data sets produced in this work may be used to develop machine learning models for predictive experimentation.

In summary, this study highlights a strategy that can be extended to other alloy systems and properties to discover new materials with enhanced functionalities.

EXPERIMENTAL APPROACH

For ease of data management, all experiments were performed with the long flat edge of the wafer positioned at the bottom. Sample pads were numbered from left to right with 1 to 5 parallel to the long flat edge and continuing to rows above (Figure S1).

Magnetron Sputtering of Thin Films. Ternary thin film composition spread between 150 and 250 nm was deposited on a 3-in. diameter thermally oxidized (2 μm SiO_2) Si wafer (thickness 400 μm, IWS) in an ultrahigh vacuum (base pressure: 5×10^{-7} Torr, 6.6×10^{-5} Pa) magnetron sputtering system at room temperature. A patterned Si mask was placed on the wafer to delineate 177 individual compositions evenly across the wafer at a Δx, Δy of 4.5 mm. High purity Ni (99.995%), Ti (99.995%), and Co (99.97%) targets (1.5 in. diameter, 0.125 in. thick, Lesker) were co-sputtered with ultrahigh purity Argon gas (99.9997%, Airgas) pressure of 5×10^{-3} Torr (0.6 Pa). The thin film library was deposited over a period of 51 min using a DC power source for Ni and Ti sputtered at 50 and 100 W, respectively, and an RF power source of 18 W for Co. The substrate was water cooled to avoid crystallization during sputter deposition and to maintain low temperatures.[60] The resulting film was annealed in a vacuum at 500 °C for 1 h.

Wavelength Dispersive Spectroscopy (WDS). Chemical composition of the Ni−Ti−Co thin film library was determined by using WDS in an electron probe microanalyzer (EPMA) JXA 8900R Microprobe, with an acceleration voltage of 15 kV. Calibration was done using polished pure metal with an experimental error margin of <0.3 at. %. WDS was selected over energy dispersive spectroscopy (EDS) due to its higher accuracy and precision in quantifying elemental content via better energy resolution from peak/background ratio.[61]

High-Throughput X-ray Diffraction (XRD) Measurements. Structural information was obtained by X-ray diffraction (XRD) measurements conducted at room temperature at SLAC National Accelerator Laboratory beamline 1−5. The 14.99 keV beam of wavelength 0.82657 Å was collimated to ∼0.3 mm × 0.3 mm. An exposure rate of 30 s was used to collect data on a MarCCD detector. A small grazing incidence angle of 1−2° was used to scan the library and minimize influence of diffraction from the silicon substrate.

Geometric parameters of 2D detector such as direct beam position, rotation, tilting, and sample to detector distance was extracted for data analysis using a LaB_6 powder pattern. These parameters were used to transform initial raw images that were acquired as a function of Q and χ in diffraction coordinate into 1D diffraction patterns by integrating and normalizing over the χ angle. Bragg angle (2θ) is related to scattering vector (Q) by the relationship $Q = 4 \times \pi \times \sin(\theta)/\lambda$, with wavelength ($\lambda$) help to generate a more traditional 1D spectrum (intensity vs 2θ). These were then analyzed using EVA4 XRD software (Bruker) and matched against the International Center for Diffraction Data (ICDD) database.[57]

Cluster Analysis of XRD data. An unsupervised machine learning algorithm was used as an exploratory data analysis tool as well as a phase mapping tool. A Pearson correlation coefficient (PCC) clustering model was applied using Combi-View, a MATLAB-supported data visualization platform developed by the Takeuchi group. It used the criteria for similarity and dissimilarity between input data such that data grouped into a cluster share similar characteristics than data in other clusters.[62] For two spectra x and y having means $\overline{x}$ and $\overline{y}$, PCC is defined as[38]

$$C_{xy} = \frac{\sum_{i=1}^{n}(x_i - \overline{x})(y_i - \overline{y})}{\left[\sum_{i=1}^{n}(x_i - \overline{x})^2 \sum_{i=1}^{n}(y_i - \overline{y})^2\right]^{1/2}}$$

This clustering model was applied to the diffraction patterns of the 177 points in the library.

High-Throughput X-ray Photoelectron Spectroscopy (XPS). XPS analyses were carried out with a Kratos Axis NOVA spectrometer using a monochromatic Al Kα source (30 mA, 15 kV). XPS can detect all elements except hydrogen and helium, probes the surface of the sample to a depth of 5−7 nm, and has detection limits ranging from 0.001 to 0.5 at. % depending on the element/matrix. The instrument work function was calibrated to give a binding energy (BE) of 83.96 eV for the Au 4f7/2 line for metallic gold and the spectrometer dispersion was adjusted to give a BE of 932.62 eV for the Cu 2p3/2 line of metallic copper. The Kratos charge neutralizer system was used on all specimens. Survey scan analyses were carried out with an analysis area of 300 × 700 μm and a pass energy of 160 eV. High resolution analyses were carried out with an analysis area of 300 × 700 μm and a pass energy of 20 eV. Spectra have been charge-corrected to the main line of the carbon 1s spectrum (adventitious carbon) set to 285.0 eV (Table 3).

Table 3. XPS Species and Associated Binding Energies

photoelectron peak	binding energy (eV)
Ni 2p	853
Co 2p	778
O 1s	530
Ti 2p	455
C 1s	285

For quantification, Shirley background subtraction removed the contribution of inelastically scattered electrons. For chemical state analysis, peaks were fitted with symmetric Gaussian−Lorentzian components using the ESCApe data system and were quantified using modified Wagner relative sensitivity factors. Spatial distribution plots were performed using the ESCApe data system whereby a series of analysis points can be created either freehand or as a grid. The spectra were analyzed as grouped data post quantification. A Delaunay triangulation is fitted onto the acquisition locations.[63] A linearly interpolated color scheme is then applied to each triangle based on the vertex values, each of which represents an acquired atomic concentration value.

Four-Point Probe Resistance−Temperature $R(T)$ Measurements. Transformation temperature parameters of A_s, A_f, M_s, M_f, and $\Delta T(A_f - M_s)$ were determined from resistance as a function of temperature $R(T)$ measurements. A customized automated four-point probe test stand developed at Ruhr Universität Bochum was used to rapidly characterize the entire library. On the basis of a measurement methodology described by van der Pauw, the test stand has a probe head mounted on a z-axis with 5 sets of four-point probes enclosed in a box purged with N_2 gas.[64,44,45] Probe tips are spaced at 500 μm and automated to measure resistance with a 50-mA current source between −40 and +120 °C with a heating/cooling rate of 5 °C/min. The library was subjected to 84 temperature cycles during this experiment.

AUTHOR INFORMATION

Corresponding Author

Ichiro Takeuchi − *Department of Materials Science and Engineering, University of Maryland, College Park, Maryland 20742, United States;* orcid.org/0000-0003-2625-0553; Email: takeuchi@umd.edu

Authors

Naila M. Al Hasan − *Department of Materials Science and Engineering, University of Maryland, College Park, Maryland 20742, United States;* orcid.org/0000-0001-8339-0187

Huilong Hou − *Department of Materials Science and Engineering, University of Maryland, College Park, Maryland 20742, United States;* orcid.org/0000-0003-0865-1142

Tieren Gao – *Department of Materials Science and Engineering, University of Maryland, College Park, Maryland 20742, United States*
Jonathan Counsell – *Kratos Analytical Limited, Manchester M17 1 GP, U.K.*
Suchismita Sarker – *Stanford Synchrotron Radiation Lightsource, SLAC National Accelerator Laboratory, Menlo Park, California 94025, United States;* orcid.org/0000-0002-8820-1143
Sigurd Thienhaus – *Materials Discovery and Interfaces, Ruhr-Universität Bochum, 44801 Bochum, Germany*
Edward Walton – *Kratos Analytical Limited, Manchester M17 1 GP, U.K.*
Peer Decker – *Materials Discovery and Interfaces, Ruhr-Universität Bochum, 44801 Bochum, Germany*
Apurva Mehta – *Stanford Synchrotron Radiation Lightsource, SLAC National Accelerator Laboratory, Menlo Park, California 94025, United States;* orcid.org/0000-0003-0870-6932
Alfred Ludwig – *Materials Discovery and Interfaces, Ruhr-Universität Bochum, 44801 Bochum, Germany;* orcid.org/0000-0003-2802-6774

Author Contributions

T.G. prepared the materials library; the manuscript and the Supporting Information were prepared with contributions from all authors. All authors have given approval to the final version of the manuscript.

Funding

N.M.A.H. acknowledges financial support by the National Science Foundation Graduate Research Fellowship Program under Grant No. DGE 1322106.

Notes

The authors declare no competing financial interest.
The raw data is available for future discussion/analysis upon request to the authors.

■ ACKNOWLEDGMENTS

The authors thank Valentin Stanev, Boian S. Alexandrov, Alan Savan, Christopher Klingshirn, Isabel Lloyd, Lourdes Salamanca-Riba, and Jason Hattrick-Simpers for fruitful discussions.

■ ABBREVIATIONS

WDS, wavelength dispersive spectroscopy; XRD, X-ray diffraction; XPS, X-ray photoelectron spectroscopy; PCC, Pearson correlation coefficient

■ REFERENCES

(1) Miyazaki, S., Fu, Y. Q., Huang, W. M., Eds., *Thin Film Shape Memory Alloys, Fundamentals and Device Applications*, 1st ed.; Cambridge University Press: Cambridge, U.K., 2009.
(2) Kornilov, I. I.; Kachur, E. V.; Belousov, O. K. Investigation of TiNi-TiCo system. *Russ. Metall.* **1975**, *2*, 162–163.
(3) Bozorth, R. M. *Ferromagnetism*; Wiley VCH - IEEE Press: 1993.
(4) Ahmad, Z.; Akbar, S.; Farooque, M.; Ul Haq, A.; Yan, M. Synthesis and magnetic properties of Nb-doped Al–Ni–Co–Ti–Cu–Fe permanent magnets. *Philos. Mag. Lett.* **2011**, *91* (3), 173–181.
(5) Belyaev, I. V.; Bazhenov, V. E.; Moiseev, A. V.; Kireev, A. V. New Fe- Co- Ni- Cu- Al- Ti Alloy for Single-Crystal Permanent Magnets. *Phys. Met. Metallogr.* **2016**, *117* (3), 214–221.
(6) Yeh, A.-C.; Chang, Y.-J.; Tsai, C.-W.; Wang, Y.-C.; Yeh, J.-W.; Kuo, C.-M. On the Solidification and Phase Stability of a Co-Cr-Fe-Ni-Ti High-Entropy Alloy. *Metall. Mater. Trans. A* **2014**, *45* (1), 184–190.
(7) Samal, S.; Rahul, M. R.; Kottada, R. S.; Phanikumar, G. Hot deformation behaviour and processing map of Co-Cu-Fe-Ni-Ti eutectic high entropy alloy. *Mater. Sci. Eng., A* **2016**, *664*, 227–235.
(8) Mohammad Sharifi, E.; Kermanpur, A. Superelastic behavior of nanostructured Ti50Ni48Co2 shape memory alloy with cold rolling processing. *Trans. Nonferrous Met. Soc. China* **2018**, *28* (7), 1351–1359.
(9) Christofidou, K. A.; Jones, N. G.; Pickering, E. J.; Flacau, R.; Hardy, M. C.; Stone, H. J. The microstructure and hardness of Ni-Co-Al-Ti-Cr quinary alloys. *J. Alloys Compd.* **2016**, *688*, 542–552.
(10) Zhong, Z.; Gu, Y.; Yuan, Y.; Yokokawa, T.; Harada, H. On the low cycle fatigue behavior of a Ni-base superalloy containing high Co and Ti contents. *Mater. Sci. Eng., A* **2012**, *552*, 434–443.
(11) Ahmed, R. A. Electrochemical Properties of Ni_{47} Ti_{49} Co_{4} Shape Memory Alloy in Artificial Urine for Urological Implant. *Ind. Eng. Chem. Res.* **2015**, *54* (34), 8397–8404.
(12) El-Bagoury, N. Microstructure and martensitic transformation and mechanical properties of cast Ni rich NiTiCo shape memory alloys. *Mater. Sci. Technol.* **2014**, *30* (14), 1795–1800.
(13) Kök, M.; Ateş, A. The effect of addition of various elements on properties of NiTi-based shape memory alloys for biomedical application. *Eur. Phys. J. Plus* **2017**, *132* (4), 6.
(14) Jing, R.; Liu, F. The Influence of Co Addition on Phase Transformation Behavior and Mechanical Properties of TiNi Alloys. *Chin. J. Aeronaut.* **2007**, *20* (2), 153–156.
(15) Soni, H.; Sannayellappa, N.; Rangarasaiah, R. M. An experimental study of influence of wire electro discharge machining parameters on surface integrity of TiNiCo shape memory alloy. *J. Mater. Res.* **2017**, *32* (16), 3100–3108.
(16) Huang, X.; Norwich, D. W.; Ehrlinspiel, M. Corrosion Behavior of Ti-55Ni-1.2Co High Stiffness Shape Memory Alloys. *J. Mater. Eng. Perform.* **2014**, *23* (7), 2630–2634.
(17) Phukaoluan, A.; Khantachawana, A.; Kaewtatip, P.; Dechkunakorn, S.; Kajornchaiyakul, J. Improvement of mechanical and biological properties of TiNi alloys by addition of Cu and Co to orthodontic archwires. *Int. Orthod.* **2016**, *14* (3), 295–310.
(18) Mohammad Sharifi, E.; Karimzadeh, F.; Kermanpur, A. Nanocrystallization of the Ti50Ni48Co2 Shape Memory Alloy by Thermomechanical Treatment. *J. Mater. Eng. Perform.* **2015**, *24* (1), 445–451.
(19) Isola, L.; La Roca, P.; Sobrero, C.; Fuster, V.; Vermaut, P.; Malarría, J. Martensitic transformation strain and stability of Ni50-x–Ti50–Cox (x = 3, 4) strips obtained by twin-roll casting and standard processing techniques. *Mater. Des.* **2016**, *107*, 511–519.
(20) Hosoda, H.; Fukul, T.; Inoue, K.; Mishima, Y.; Suzuki, T. Change of Ms Temperatures and its Correlation to Atomic Configurations of Offstoichiometric NiTi-Cr and NiTi-Co Alloys. *MRS Proc.* **1996**, *459*, 287.
(21) Civjan, S.; Huget, E. F.; DeSimon, L. B. Potential Applications of Certain Nickel-Titanium (Nitinol) Alloys. *J. Dent. Res.* **1975**, *54* (1), 89–96.
(22) Kishi, Y.; Yajima, Z.; Shimizu, K. Relation between Tensile Deformation Behavior and Microstructure in a Ti-Ni-Co Shape Memory Alloy. *Mater. Trans.* **2002**, *43* (5), 834–839.
(23) Hosoda, H.; Hanada, S.; Inoue, K.; Fukui, T.; Mishima, Y.; Suzuki, T. Martensite transformation temperatures and mechanical properties of ternary NiTi alloys with offstoichiometric compositions. *Intermetallics* **1998**, *6* (4), 291–301.
(24) Bechtold, C.; Chluba, C.; Lima de Miranda, R.; Quandt, E. High cyclic stability of the elastocaloric effect in sputtered TiNiCu shape memory films. *Appl. Phys. Lett.* **2012**, *101* (9), 091903.
(25) Larnicol, M.; Portier, R.; Ochin, P. Influence of Rapid Solidification on Ni50-xTi50Cx Shape Memory Alloys. *J. Phys. IV* **1997**, *07*, C5-191.

(26) Alqarni, N. D.; Wysocka, J.; El-Bagoury, N.; Ryl, J.; Amin, M. A.; Boukherroub, R. Effect of cobalt addition on the corrosion behavior of near equiatomic NiTi shape memory alloy in normal saline solution: electrochemical and XPS studies. *RSC Adv.* **2018**, *8* (34), 19289−19300.
(27) Soni, H.; Narendranath, S.; Ramesh, M. R. Effects of Wire Electro-Discharge Machining Process Parameters on the Machined Surface of Ti 50 Ni 49 Co 1 Shape Memory Alloy. *Silicone* **2018**, *5*, 19166.
(28) Mohammad Sharifi, E.; Kermanpur, A.; Karimzadeh, F. The effect of thermomechanical processing on the microstructure and mechanical properties of the nanocrystalline TiNiCo shape memory alloy. *Mater. Sci. Eng., A* **2014**, *598*, 183−189.
(29) Fasching, A.; Norwich, D.; Geiser, T.; Paul, G. W. An Evaluation of a NiTiCo Alloy and its Suitability for Medical Device Applications. *J. Mater. Eng. Perform.* **2011**, *20* (4−5), 641−645.
(30) Goryczka, T.; Ochin, P.; Lelątko, J. Shape Memory Effect in NiTiCo Strip Produced by Twin Roll Casting Technique. *Mater. Sci. Forum* **2013**, *738−739*, 348−351.
(31) Jordan, L.; Goubaa, K.; Masse, M.; Bouquet, G. Comparitive study of mechanical properties of various Ni-Ti based shape memory alloys in view of dental and medical applications. *J. Phys. IV* **1991**, *01* (C4), C4-139−C4-144.
(32) Martins, R. M. S.; Schell, N.; von Borany, J.; Mahesh, K. K.; Silva, R. J. C.; Braz Fernandes, F. M. Structural evolution of magnetron sputtered shape memory alloy Ni−Ti films. *Vacuum* **2010**, *84* (7), 913−919.
(33) Gupta, K. P. The Co-Ni-Ti System (Cobalt-Nickel-Titanium). *J. Phase Equilib.* **1999**, *20* (1), 65−72.
(34) Santosh, S.; Sampath, V. Effect of Ternary Addition of Cobalt on Shape Memory Characteristics of Ni−Ti Alloys. *Trans. Indian Inst. Met.* **2019**, *72*, 1481−1484.
(35) Zhou, C.; Guo, C.; Li, J.; Li, C.; Du, Z. Experimental investigations of the Co−Ni−Ti system: Liquidus surface projection and isothermal section at 1373 K. *J. Alloys Compd.* **2018**, *754*, 268−282.
(36) Gebhardt, T.; Music, D.; Takahashi, T.; Schneider, J. M. Combinatorial thin film materials science: From alloy discovery and optimization to alloy design. *Thin Solid Films* **2012**, *520* (17), 5491−5499.
(37) Takeuchi, I.; Lauterbach, J.; Fasolka, M. J. Combinatorial materials synthesis. *Mater. Today* **2005**, *8* (10), 18−26.
(38) Hattrick-Simpers, J.; et al. Rapid structural mapping of ternary metallic alloy systems using the combinatorial approach and cluster analysis. *Rev. Sci. Instrum.* **2007**, *78* (7), 072217.
(39) Long, C. J.; Bunker, D.; Li, X.; Karen, V. L.; Takeuchi, I. Rapid identification of structural phases in combinatorial thin-film libraries using x-ray diffraction and non-negative matrix factorization. *Rev. Sci. Instrum.* **2009**, *80* (10), 103902.
(40) Alqarni, N. D.; Wysocka, J.; El-Bagoury, N.; Ryl, J.; Amin, M. A.; Boukherroub, R. Effect of cobalt addition on the corrosion behavior of near equiatomic NiTi shape memory alloy in normal saline solution: electrochemical and XPS studies. *RSC Adv.* **2018**, *8* (34), 19289−19300.
(41) Firstov, G.; Vitchev, R.; Kumar, H.; Blanpain, B.; Van Humbeeck, J. Surface oxidation of NiTi shape memory alloy. *Biomaterials* **2002**, *23* (24), 4863−4871.
(42) Zheng, Y. F.; Wang, B. L.; Wang, J. G.; Li, C.; Zhao, L. C. Corrosion behaviour of Ti−Nb−Sn shape memory alloys in different simulated body solutions. *Mater. Sci. Eng., A* **2006**, *438-440*, 891−895.
(43) König, D.; Naujoks, D.; de los Arcos, T.; Grosse-Kreul, S.; Ludwig, A. X-Ray Photoelectron Spectroscopy Investigations of the Surface Reaction Layer and its Effects on the Transformation Properties of Nanoscale Ti51Ni38Cu11 Shape Memory Thin Films. *Adv. Eng. Mater.* **2015**, *17* (5), 669−673.
(44) Thienhaus, S.; Zamponi, C.; Rumpf, H.; Hattrick-Simpers, J.; Takeuchi, I.; Ludwig, A. High-throughput characterization of shape memory thin films using automated temperature-dependent resistance measurements. *MRS Proc.* **2005**, *894*, LL06-06.
(45) Thienhaus, S.; Hamann, S.; Ludwig, A. Modular high-throughput test stand for versatile screening of thin-film materials libraries. *Sci. Technol. Adv. Mater.* **2011**, *12* (5), 054206.
(46) Wu, Y.; Ertekin, E.; Sehitoglu, H. Elastocaloric cooling capacity of shape memory alloys − Role of deformation temperatures, mechanical cycling, stress hysteresis and inhomogeneity of transformation. *Acta Mater.* **2017**, *135*, 158.
(47) Planes, A.; Flores-Zúñiga, H.; Soto-Parra, D.; Vives, E.; Matutes-Aquino, J. A.; Mañosa, L. Elastocaloric effect in Ti-Ni shape-memory wires associated with the B2 ↔ B19' and B2 ↔ R structural transitions. *Appl. Phys. Lett.* **2016**, *108* (7), 071902.
(48) Gutfleisch, O.; Gottschall, T.; Fries, M.; Benke, D.; Radulov, I.; Skokov, K. P.; Wende, H.; Gruner, M.; Acet, M.; Entel, P.; et al. Mastering hysteresis in magnetocaloric materials. *Philos. Trans. R. Soc., A* **2016**, *374* (2074), 20150308.
(49) Stern-Taulats, E.; Castán, T.; Mañosa, L.; Planes, A.; Mathur, N. D.; Moya, X. Multicaloric materials and effects. *MRS Bull.* **2018**, *43* (4), 295−299.
(50) Cui, J.; et al. Combinatorial search of thermoelastic shape-memory alloys with extremely small hysteresis width. *Nat. Mater.* **2006**, *5* (4), 286−90.
(51) Ingale, B. D.; Wei, W. C.; Chang, P. C.; Kuo, Y. K.; Wu, S. K. Anomalous transport and thermal properties of NiTi and with Cu and Fe-doped shape memory alloys near the martensitic transition. *J. Appl. Phys.* **2011**, *110*, 113721.
(52) Isola, L.; et al. Load-biased martensitic transformation strain of Ti50−Ni47−Co3 strip obtained by a twin-roll casting technique. *Mater. Sci. Eng., A* **2014**, *597*, 245−252.
(53) Naresh, H.; Bharath, H. S.; Prashantha, S. The Influence of Alloying Constituent Fe on Mechanical Properties Of NiTi Based Shape Memory Alloys. *Mater. Today Proc.* **2017**, *4* (10), 11251−11259.
(54) Honma, T. *Types of Mechanical Characteristics of Shape Memory Alloys: TiNi−Based Shape Memory Alloys*; Shape Memory Alloys; Gordon and Breach Science Publishers: New York, 1987.
(55) Liu, F.; Ding, Z.; Li, Y.; Xu, H. Phase transformation behaviors and mechanical properties of TiNiMo shape memory alloys. *Intermetallics* **2005**, *13* (3−4), 357−360.
(56) Long, C. J. *CombiView download*; SourceForge.net: 2015. [Online]. Available: https://sourceforge.net/projects/xrdsuite/. [Accessed: 06-Jan-2020].
(57) *DIFFRAC.SUITE EVA - XRD Software*; Bruker: [Online]. Available: https://www.bruker.com/products/x-ray-diffraction-and-elemental-analysis/x-ray-diffraction/xrd-software/eva.html. [Accessed: 13-Apr-2020].
(58) Zarnetta, R.; et al. Identification of quaternary shape memory alloys with near-zero thermal hysteresis and unprecedented functional stability. *Adv. Funct. Mater.* **2010**, *20* (12), 1917−1923.
(59) Wieczorek, A.; et al. Thermal Stabilization of NiTiCuV Shape Memory Alloys: Observations During Elastocaloric Training. *Shape Mem. Superelasticity* **2015**, *1* (2), 132−141.
(60) Cho, H.; Kim, H. Y.; Miyazaki, S. Fabrication and characterization of Ti−Ni shape memory thin film using Ti/Ni multilayer technique. *Sci. Technol. Adv. Mater.* **2005**, *6* (6), 678−683.
(61) Goldstein, J., Ed., *Scanning electron microscopy and X-ray microanalysis: A text for biologists, materials scientists, and geologists*; Plenum Publishing Corporation: 1992.
(62) Mueller, T.; Kusne, A.; Ramprasad, R. Machine Learning in Materials Science: Recent Progress and Emerging Applications,. *Reviews in Computational Chemistry* **2016**, *29*, 186−273.
(63) Delaunay, B. Sur la sphère vide. A la mémoire de Georges Voronoï. Classe des sciences mathématiques et naturelles. *Bull. Acad. URSS* **1934**, *6*, 793−800.
(64) van der Pauw, L. J. A method of measuring specific resistivity and Hall effect of discs of arbitray shape. *Philips Res. Rep.* **1958**, *13*, 1.